Front. Chem. Sci. Eng. 2023, 17(5): 606–616
https://doi.org/10.1007/s11705-022-2233-4

RESEARCH ARTICLE

Design and synthesis of $ZnCo_2O_4$/CdS for substantially improved photocatalytic hydrogen production

Xiaohong Li[1], **Youji Li** (✉)[2], **Xin Guo**[1], **Zhiliang Jin** (✉)[1]

1 School of Chemistry and Chemical Engineering, North Minzu University, Yinchuan 750021, China
2 College of Chemistry and Chemical Engineering, Jishou University, Jishou 416000, China

Abstract In this study, the hydrogen evolution performance of CdS nanorods is improved using $ZnCo_2O_4$. $ZnCo_2O_4$ nanospheres are synthesized using the hydrothermal and calcination methods, and CdS nanorods are synthesized using the solvothermal method. From the perspective of morphology, numerous CdS nanorods are anchored on the $ZnCo_2O_4$ microspheres. According to the experimental results of photocatalytic hydrogen evolution, the final hydrogen evolution capacity of 7417.5 $\mu mol \cdot g^{-1} \cdot h^{-1}$ is slightly more than two times that of the single CdS, which proves the feasibility of our study. Through various characterization methods, it is proved that the composite sample has suitable optoelectronic properties. In addition, $ZnCo_2O_4$ itself exhibits good conductivity and low impedance, which shortens the charge-transfer path. Overall, the introduction of $ZnCo_2O_4$ expands the adsorption range of light and improves the performance of photocatalytic hydrogen evolution. This design can provide reference for developing high-efficiency photocatalysts.

Keywords $ZnCo_2O_4$ nanosphere, CdS nanorods, photocatalytic hydrogen evolution

1 Introduction

The conversion of fuel into solar energy has greatest potential for achieving the goal of a low-carbon economy [1–6]. In particular, photocatalytic cracking of water is a primary measure adopted to generate clean, efficient, green, and storable hydrogen energy [3,7–14]. However, in many semiconductor photocatalysts, due to their limitations of low activity, poor stability, fast recombination of photogenerated carriers, and narrow light absorption range, the unmodified single catalysts are not ideal for photocatalytic hydrogen evolution [15–20].

Among the many candidate photocatalysts, CdS has been widely used in various photocatalytic reactions because of its suitable band gap and low-cost synthesis [21]. Moreover, the ingenious coupling of hybrid metal sulfides can expand the absorption band of the solar spectrum and exhibit appropriate redox potential [22]. However, CdS suffers from the shortcomings of photoetching, instability, and annihilation of electron–hole pairs [1,23]. To overcome these, a reasonable photocatalyst design is required. Among many methods, such as heterojunction construction, surface modification, and defect engineering, co-catalyst loading is an effective method to address this problem and achieve efficient hydrogen evolution [24–26]. Therefore, in this study, we combine CdS with a co-catalyst to overcome the demerits of CdS. Certain precious metals can act as effective co-catalysts because of their good conductivity and high electron density. However, their high cost limits their wide application [27,28]. Therefore, it is critical to identify non-precious metal co-catalysts such as sulfides, phosphates, transition metal oxides and carbon-based materials, which have been widely used [29,30]. Among them, the transition metal oxide $ZnCo_2O_4$ has attracted much attention because of its large specific surface area, suitable electrochemical performance, environment-friendliness and morphological diversity. The synthesis strategies are different, and the prepared $ZnCo_2O_4$ includes nano-blocks, nano-microsphere, nanosheets and nanowires [31–33]. Because of its various forms, $ZnCo_2O_4$ has been widely used in electrochemistry and capacitor electrode materials. However, it is rarely used in photocatalytic hydrogen production.

To improve the photocatalytic hydrogen evolution performance of CdS, this study constructs a composite photocatalyst $ZnCo_2O_4$/CdS by using $ZnCo_2O_4$ as a co-catalyst. The appropriate interface between $ZnCo_2O_4$ and CdS accelerates the electron transfer, improves the light absorption efficiency, and thus, enhances the hydrogen

Received June 2, 2022; accepted August 10, 2022

E-mails: bcclyj@163.com (Li Y.), zl-jin@nun.edu.cn (Jin Z.)

evolution performance. Thus, this study is expected to contribute to the design of co-catalysts.

2 Experimental

2.1 Synthesis of $ZnCo_2O_4$ catalyst

First, 0.58 g of $Co(NO_3)_2 \cdot 6H_2O$, 0.29 g of $Zn(NO_3)_2 \cdot 6H_2O$, 0.07 g of NH_4F, and 0.30 g of $CO(NH_2)_2$ were dispersed into 35 mL of deionized water. After stirring in a magnetic agitator for 1 h, the mixed solution was transferred to a 50 mL autoclave lined with Teflon at 120 °C and maintained at this temperature for 5 h. At the end of the reaction, the products were collected, washed with deionized water and ethanol three times, and then dried. Finally, the dried sample was calcined in air at 400 °C for 2 h at a rate of 5 °C·min^{-1}. The black powder obtained by calcination was named ZCO.

2.2 Synthesis of CdS catalyst

First, 3.68 g of $Cd(NO_3)_2$ was added to 50 mL of ethylenediamine and stirred for 1 h. Then, 2.85 g of thiourea was added to the solution and stirred for another 1 h. Next, the solution was transferred to a 100 mL autoclave lined with polytetrafluoroethylene under a reaction temperature of 160 °C and reaction time of 24 h. After the reaction, the product was washed with ethanol and deionized water, and then dried. The finally obtained yellow sample was CdS.

2.3 Preparation of composite materials

The composite catalyst was prepared using a simple physical mixing method. First, 0.005 g of $ZnCo_2O_4$ was added to a beaker containing 0.1 g of CdS and 30 mL of alcohol. After ultrasonic treatment for 10 min, the solution was stirred and dried in a water bath. The composite catalyst was named 5%-ZCOCS. Under the same conditions, the composite catalysts with the proportions of 10%-ZCOCS, 15%-ZCOCS, and 20%-ZCOCS were synthesized.

2.4 Photocatalytic hydrogen evolution experiments

The experiment of photocatalytic hydrogen evolution was conducted in a closed glass bottle by using a 5 W white-light multi-channel photocatalytic reaction system. First, we added 10 mg of the catalyst and 30 mL of 10% lactic acid to the glass bottle, stirred the solution for 5 min, and then removed air from the glass bottle with nitrogen. After that, 0.5 mL of the gas was extracted from the glass bottle every hour and detected and analyzed by gas chromatography. The photocatalytic hydrogen evolution stability test was conducted every 4 h, with a total of four cycles.

2.5 Characterization

The crystal structure of the sample was analyzed by powder X-ray diffraction (XRD) under Cu-Kα radiation. The morphology of the sample was analyzed using a scanning electron microscope (SEM, Zeiss Evo 10) and a transmission electron microscope (TEM, Tecnai G2-TF30). The elemental composition and chemical state of the sample were analyzed by X-ray photoelectron spectroscopy (XPS, ESCALAB 250Xi). The adsorption and desorption isotherms of nitrogen were measured using ASAP 2020 M. The results were analyzed by the Brunauer–Emmett–Teller (BET) equation. The Barrett–Joyner–Halenda (BJH) model was used to analyze the pore size distribution curve. Taking $BaSO_4$ as the reference, the UV–Visible diffuse reflectance spectrum (UV–Vis DRS) of the sample was measured using a UV-2550 spectrometer. The photoluminescence (PL) spectra and time-resolved fluorescence (TRPL) spectra were obtained using FluoroMAX-4.

3 Results and discussion

3.1 XRD analysis

The crystal structure of the catalyst is analyzed by XRD. In Fig. 1, the diffraction peaks at 31.26°, 36.71°, 44.77°, 59.26° and 65.15° belong to the (220), (311), (400), (511), and (440) crystal faces of $ZnCo_2O_4$ (JCPDS No. 23-1390), respectively. The characteristic diffraction peaks of CdS (JCPDS No. 41-1049) are observed at 24.83°, 26.58°, 28.21°, 36.71°, 43.68°, 47.82°, and 51.85°, corresponding to their (100), (002), (101), (102), (110), (103), and (112) crystal planes. In addition to the evident diffraction peaks, the small diffraction peaks also

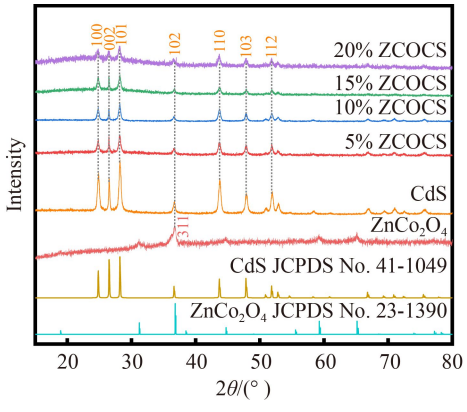

Fig. 1 Pure $ZnCo_2O_4$, CdS and different proportions of XRD patterns.

correspond well with the standard card, indicating that CdS has suitable crystallinity. The XRD diagram of the composite catalysts is also shown, where the diffraction peaks of CdS and $ZnCo_2O_4$ appear in the diffraction peak of the composite catalyst. There is no new diffraction peak, which indicates that the composite is of high purity and is successfully prepared by CdS and $ZnCo_2O_4$.

3.2 SEM and TEM analyses

The morphology and structure of the catalyst are characterized using SEM and TEM, respectively (as shown in Fig. 2). As shown in Fig. 2(a), CdS exhibits a rod-like structure. Further zooming-in the figure, clearly shows that the surface of the rod-like structure of CdS is relatively smooth and different in length (Fig. 2(b)). Figure 2(c) shows $ZnCo_2O_4$ nanospheres formed by the accumulation of rods, and Fig. 2(d) shows the SEM image of the composite sample. The large $ZnCo_2O_4$ nanospheres adsorb many CdS nanorods.

The TEM image is used to further understand the sample's microstructure, as shown in Figs. 2(e, f). Under the TEM, large $ZnCo_2O_4$ nanospheres are observed to be tightly packed black parts, while CdS appears as surrounding dispersed nanorods. Figure 2(f) shows the image obtained by magnifying the edges of the contact between the two. In the enlarged image, CdS appears to be smooth, while the rods that from the $ZnCo_2O_4$ nanospheres are not smooth. Figure 2(g) indicates a HRTEM image, which shows the lattice stripes of CdS and $ZnCo_2O_4$, where the lattice fringe spacing of 0.34 nm belongs to the (002) plane of CdS, and that of 0.24 nm corresponds to the (311) plane of $ZnCo_2O_4$. In addition, the energy-dispersive X-ray (EDX) images of Fig. 2(h) show the presence of Zn, Co, S, Cd, and O elements in the composite sample. The successful preparation of the composite sample is further illustrated.

3.3 XPS analysis

The chemical states of the elements present in the samples are studied by XPS (as shown in Fig. 3). In the full spectrum shown in Fig. 3(a), all elements of pure CdS and $ZnCo_2O_4$ can be observed in the composite sample

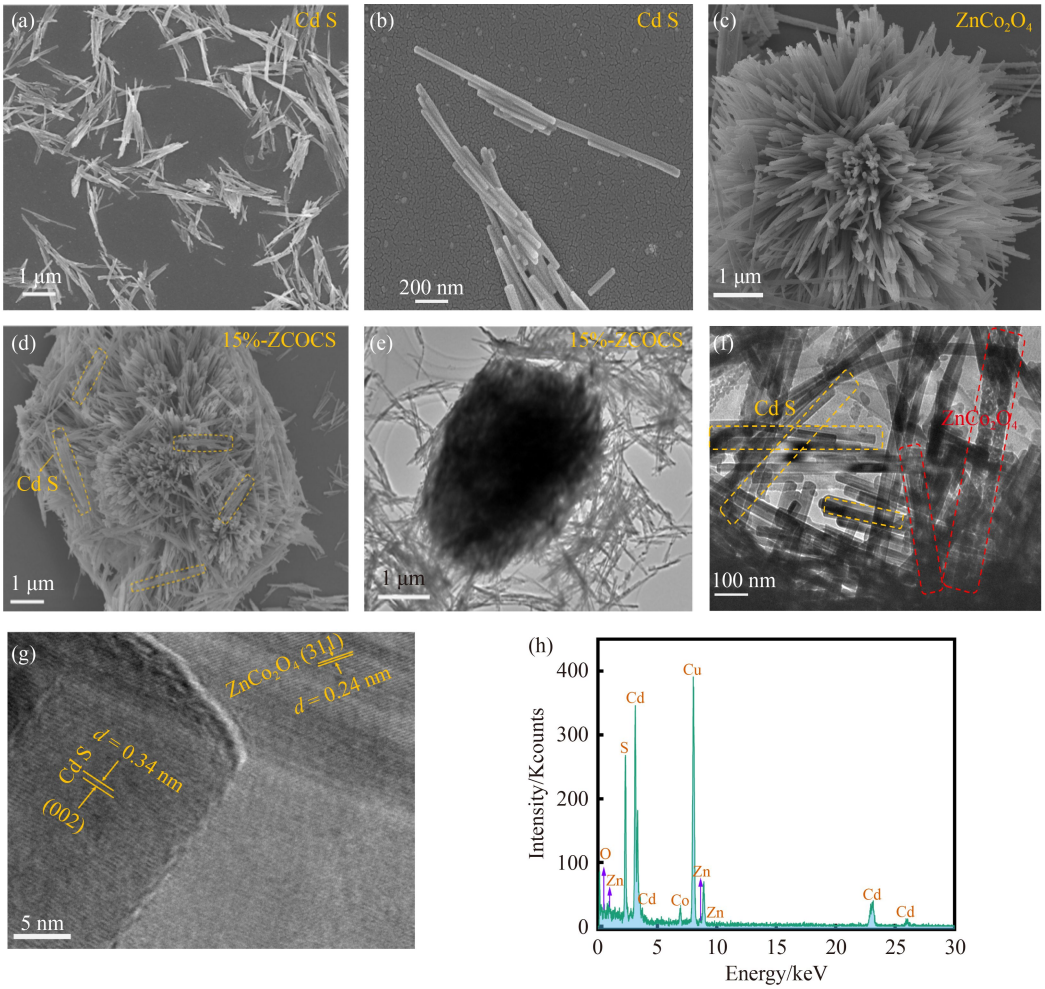

Fig. 2 SEM images of (a, b) CdS, (c) $ZnCo_2O_4$, (d) 15%-ZCOCS; TEM images of (e, f) 15%-ZCOCS; high-resolution electron microscope (HRTEM) image of (g) 15%-ZCOCS; EDX image of (h) 15%-ZCOCS.

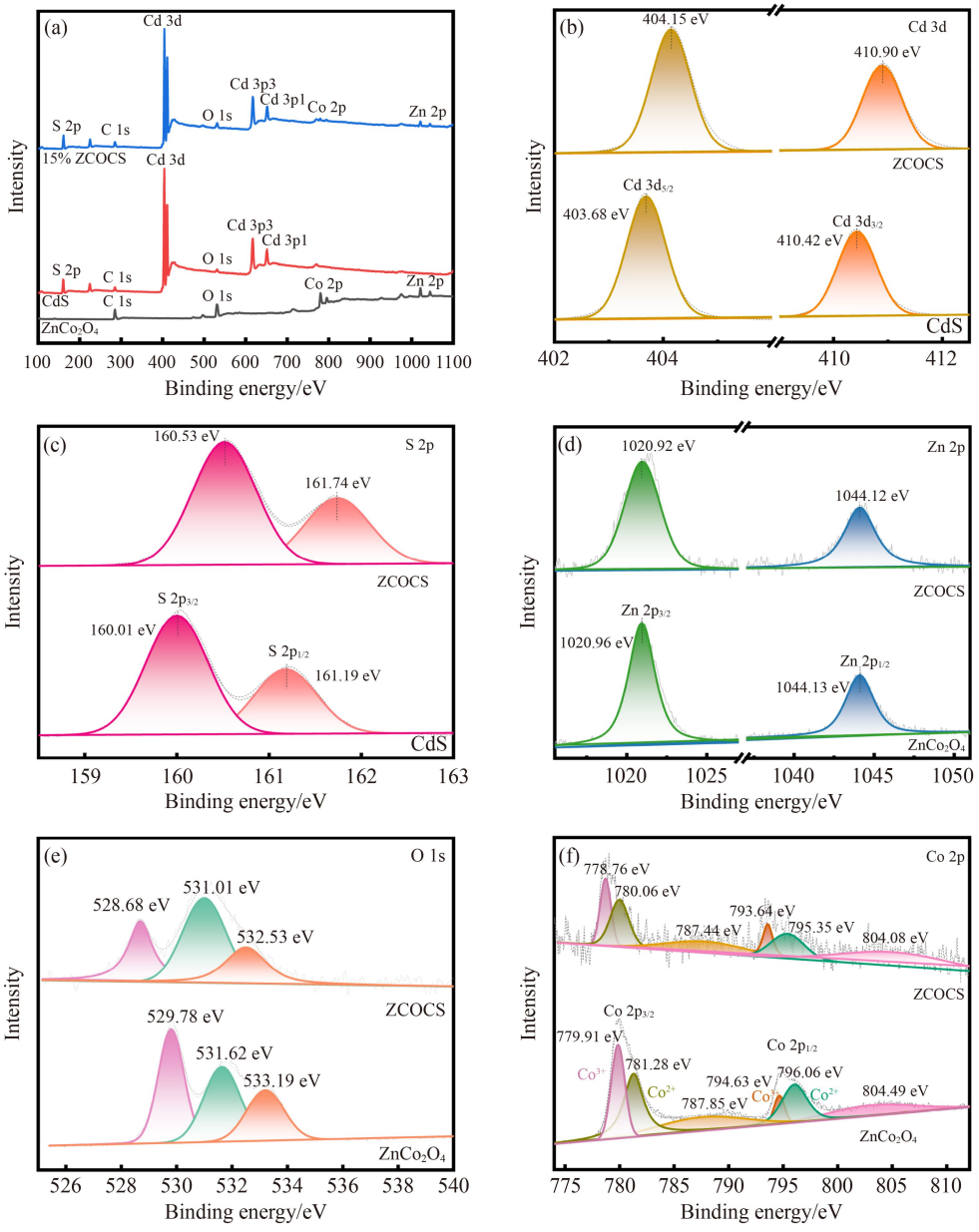

Fig. 3 (a) XPS spectra of $ZnCo_2O_4$, CdS and ZCOCS; high-resolution XPS spectra of (b) Cd 3d, (c) S 2p, (d) Zn 2p, (e) O 1s, and (f) Co 2p.

ZCOCS. Figures 3(b–f) further show the high-resolution XPS spectra of Cd 3d, S 2p, Zn 2p, O 1s, and Co 2p. As shown in Fig. 3(b), in the Cd 3d XPS spectrum of CdS, the peaks with binding energies of 404.15 and 410.90 eV correspond to Cd $3d_{5/2}$ and Cd $3d_{3/2}$, respectively [34]. In addition, the binding energies of 160.01 and 161.19 eV correspond to S $2p_{3/2}$ and S $2p_{1/2}$, respectively (Fig. 3(c)) [35]. Clearly, with the addition of $ZnCo_2O_4$, the peaks of elements Cd and S move in the direction of a large binding energy. Figures 3(d) and 3(e) show high-resolution XPS spectra of O and Zn. For Zn, the peaks are Zn $2p_{3/2}$ (1020.92 eV) and Zn $2p_{1/2}$ (1044.13 eV) [36]. The binding energy at 529.78 eV belongs to the Co–O bond [37]. In addition, the peaks at 531.62 and 533.19 eV are attributed to the surface hydroxyl groups and the O–H species absorbed water on the surface, respectively [38,39]. Moreover, the high-resolution XPS spectrum of Co (Fig. 3(f)) presents two sets of double peaks in the spin orbit and two satellite peaks. The first group comprises the binding energies of 779.91 and 781.28 eV, and the second group comprises 794.63 and 796.06 eV, which belong to Co $2p_{3/2}$ and Co $2p_{1/2}$, respectively. The binding energies of 779.91 and 794.63 eV belong to Co^{3+}, while those of 781.28 and 796.06 eV belong to Co^{2+} [38,40,41]. The satellite peaks are located at 787.85 and 804.49 eV respectively. Compared to pure CdS and pure $ZnCo_2O_4$, the binding energy of each element in the composite sample ZCOCS shifts in varying degrees,

which indicates the presence of an interaction force between CdS and $ZnCo_2O_4$.

3.4 BET analysis

The specific surface area and pore size distribution of the samples are analyzed through nitrogen adsorption–desorption curves (Fig. 4). The nitrogen adsorption–desorption curves of all three samples in Fig. 4(a), Fig. 4(b) and Fig. 4(c) are type IV isotherm and H_3 hysteresis ring [42]. Each illustration shows the pore size distribution curves obtained by the BJH method. As shown in the figure, the pore size distribution ranges within 2–50 nm, which belongs to mesoporous materials. According to the results of the BET analysis, the specific surface areas of $ZnCo_2O_4$, CdS and 15%-ZCOCS are 49, 35 and 39 $m^2 \cdot g^{-1}$, respectively (Table 1). The specific surface area of the composite sample is slightly higher than that of the single CdS. An increase in this area can expose more active sites, which is beneficial to the hydrogen evolution reaction. On the other hand, the change in adsorption parameters also indicates the successful preparation of the catalyst.

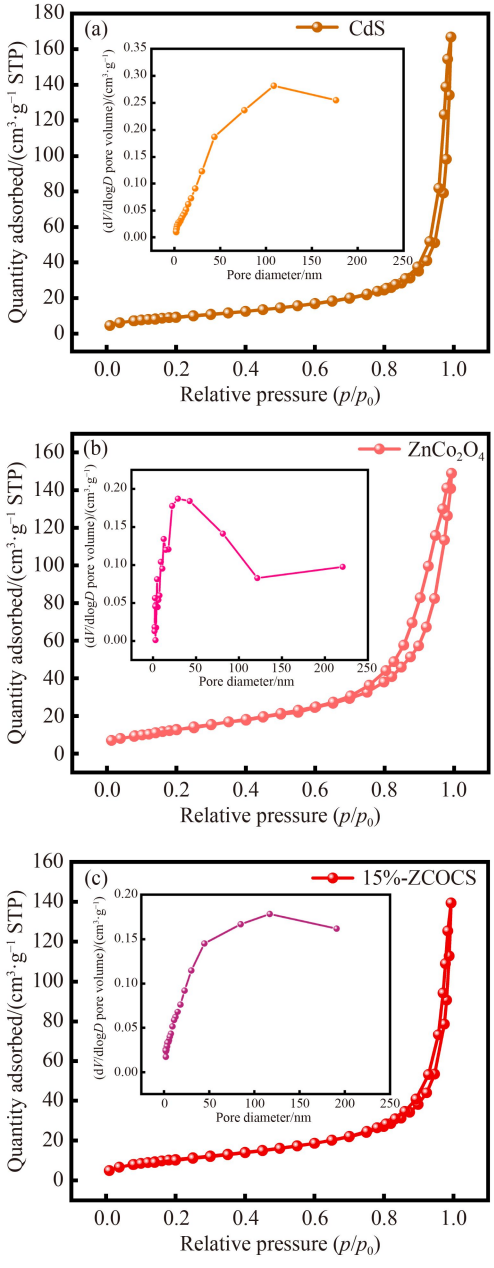

Fig. 4 Nitrogen adsorption–desorption isotherms of (a) CdS, (b) $ZnCo_2O_4$, and (c) 15%-ZCOCS.

3.5 Photocatalytic hydrogen evolution

The hydrogen evolution performance of the sample under visible light irradiation (as shown in Fig. 5). Figure 5(a) compares the photocatalytic hydrogen evolution properties of CdS, $ZnCo_2O_4$ and the composite sample ZCOCS. Due to the rapid recombination of photogenerated carriers, $ZnCo_2O_4$ shows very low photocatalytic activity for hydrogen evolution. After the introduction of $ZnCo_2O_4$, the hydrogen production capacity of CdS is improved, and the amount of hydrogen evolution can reach 7417.5 $\mu mol \cdot g^{-1} \cdot h^{-1}$, which is approximately 2.1 times that of CdS. Figure 5(b) compares the hydrogen evolution performance of different proportions of composite catalysts. As shown in the figure, the amount of hydrogen evolution differs with the addition of different loading amount of $ZnCo_2O_4$, and when the ratio of $ZnCo_2O_4$ to CdS is 20%, the amount of hydrogen evolution decreases. When the radio of $ZnCo_2O_4$ to CdS is 15%, the composite sample exhibits the optimal light absorption characteristics and suitable charge separation efficiency. The test of photocatalytic stability is another key point. Under the same conditions, after four times of hydrogen production, the composite catalyst exhibits suitable stability but the hydrogen production decreases a little due to the slight photocorrosion of the sulfide system [1,35]. Figure 5(d) shows the XRD diagram before and after hydrogen production. No miscellaneous peaks are observed in the XRD characteristic peak before and after the reaction, which shows that the structure is relatively stable. Furthermore, we reviewed some related studies on non-precious metal co-catalyst modified CdS for photocatalytic hydrogen evolution and compared them with our study, as shown in Table 2.

Table 1 Adsorption parameters of samples

Sample	S_{BET}/ ($m^2 \cdot g^{-1}$)	Pore volume/ ($cm^3 \cdot g^{-1}$)	Average pore size/nm
CdS	35	0.26	28.52
$ZnCo_2O_4$	49	0.23	16.27
15%-ZCOCS	39	0.22	21.39

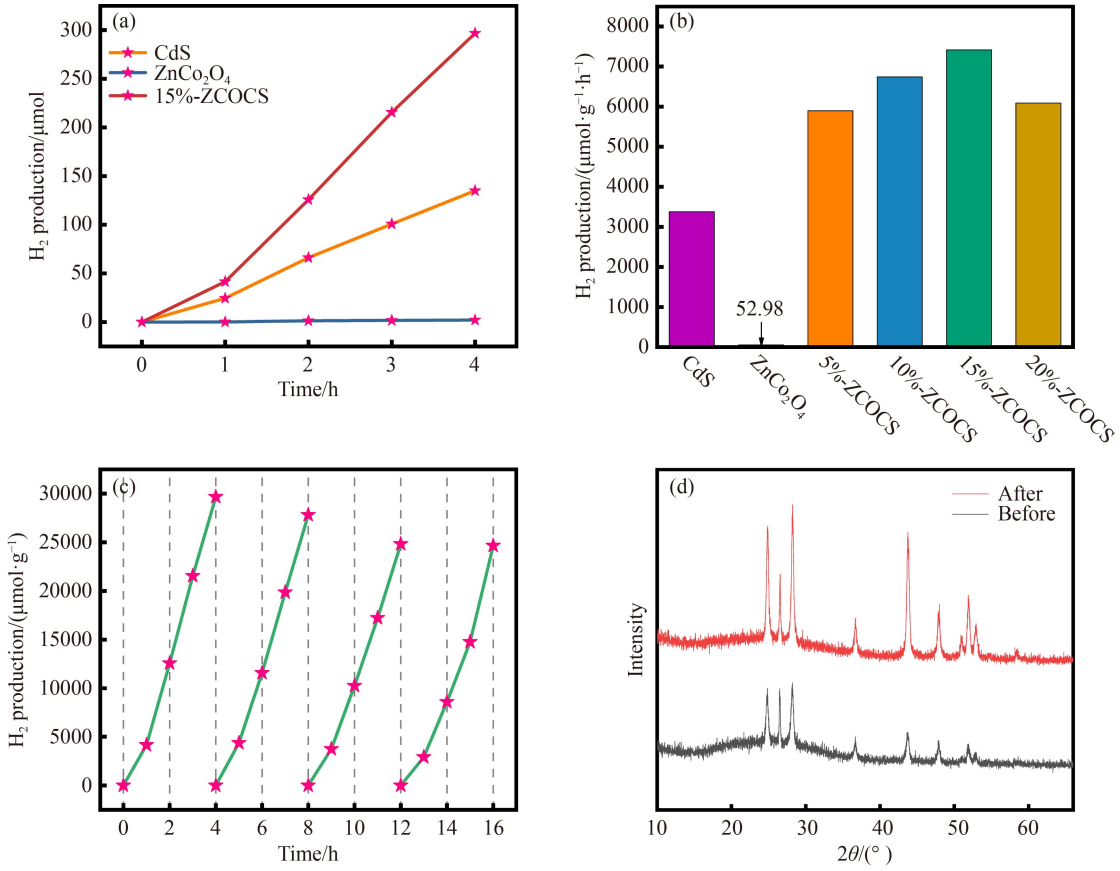

Fig. 5 (a) Photocatalytic activities of CdS, $ZnCo_2O_4$ and 15%-ZCOCS, (b) comparison of hydrogen production under different ratios, (c) 15%-ZCOCS hydrogen production cycle test, (d) XRD diagram before and after hydrogen production.

Table 2 Comparison of our study with the photocatalytic hydrogen production of CdS modified by other non-precious metals as co-catalysts

Composite photocatalyst	Sacrificial agent	Light source	Hydrogen evolution rate/(μmol·g^{-1}·h^{-1})	Ref.
Mo_2N/CdS	Na_2S/Na_2SO_3	300 W Xe Lamp	970	[43]
$NiCo_2S_4$/CdS	Lactic acid	300 W Xe Lamp	6850	[44]
Mo_2C/CdS	Na_2S/Na_2SO_3	300 W Xe Lamp	1610	[45]
VN/CdS	10 vol % latic acid	300 W Xe Lamp	6240	[46]
$Cr_{0.5}Ti_{0.5}N$/CdS	10 vol % latic acid	300 W Xe Lamp	2440	[47]
$ZnCo_2O_4$/CdS	10 vol % latic acid	5W white light	7417	This work

3.6 UV–Vis DRS and PL analyses

The light absorption properties of the samples are evaluated by UV–Vis DRS (as shown in Fig. 6). In Fig. 6(a), the black catalyst $ZnCo_2O_4$ exhibits suitable light absorption properties. The absorption edge of pure CdS nanorods is approximately 543 nm. Compared to CdS, the composite sample 15%-ZCOCS exhibits slightly stronger light absorption intensity and similar absorption band edge. This shows that the introduction of $ZnCo_2O_4$ helps to enhance the absorption of visible light. In addition, the bandgap widths of CdS and $ZnCo_2O_4$ are estimated by $(\alpha hv)^{1/n} = A(hv–E_g)$. As shown in Fig. 6(b), the bandgap width of CdS is 2.32 eV and that of $ZnCo_2O_4$ is 1.60 eV [48].

Figure 6(c) shows the PL spectra of CdS, $ZnCo_2O_4$ and different composite catalysts excited at the same wavelength. The important information reflected by the PL spectrum is the fluorescence intensity of photogenerated electron–hole pairs recombination. The figure clearly shows that the fluorescence intensity of CdS is very strong, indicating a high recombination rate of electron–hole pairs. The fluorescence intensity of the composite sample with different ratios is lower than that of CdS, indicating that the introduction of $ZnCo_2O_4$ can effectively inhibit the recombination of the electron holes, which is more conducive to a good photocatalytic hydrogen evolution reaction. In addition, the TRPL spectra of CdS, $ZnCo_2O_4$ and the different ratios of composite catalysts are also studied, as shown in Fig. 6(d). The

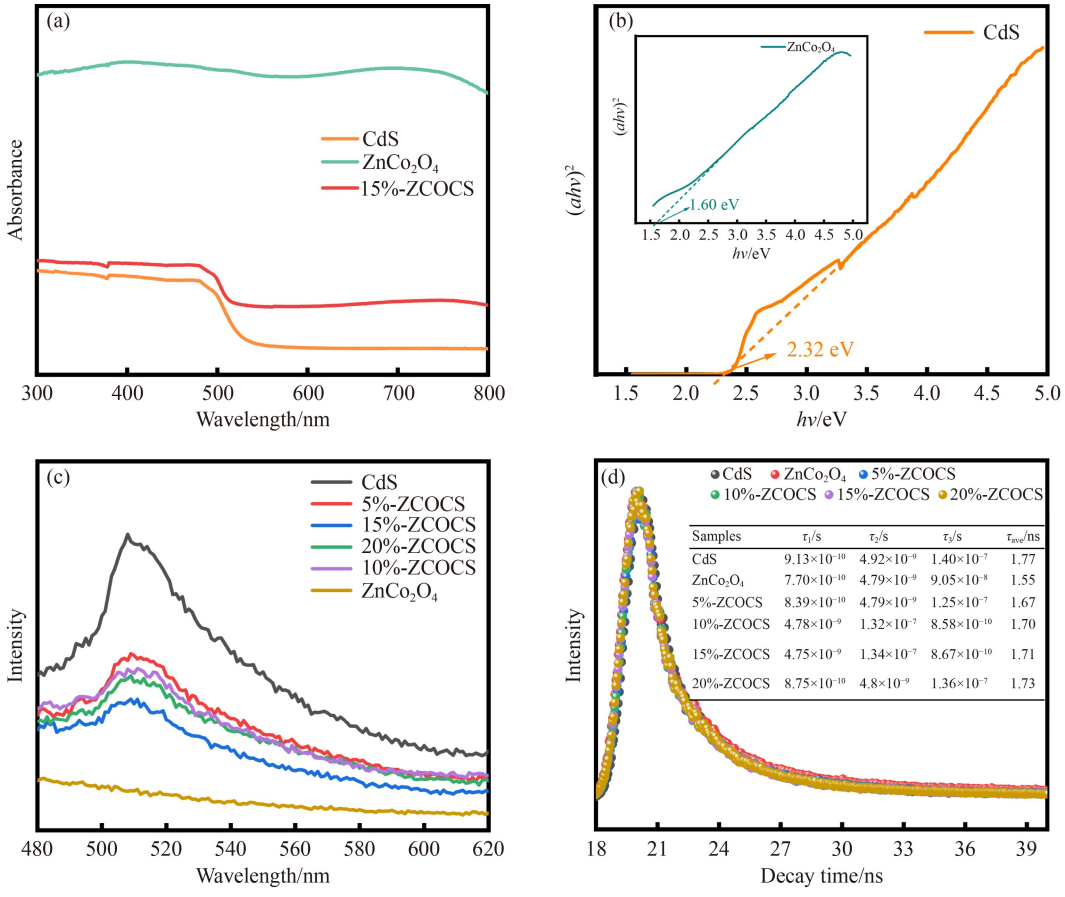

Samples	τ_1/s	τ_2/s	τ_3/s	τ_{ave}/ns
CdS	9.13×10^{-10}	4.92×10^{-9}	1.40×10^{-7}	1.77
$ZnCo_2O_4$	7.70×10^{-10}	4.79×10^{-9}	9.05×10^{-8}	1.55
5%-ZCOCS	8.39×10^{-10}	4.79×10^{-9}	1.25×10^{-7}	1.67
10%-ZCOCS	4.78×10^{-9}	1.32×10^{-7}	8.58×10^{-10}	1.70
15%-ZCOCS	4.75×10^{-9}	1.34×10^{-7}	8.67×10^{-10}	1.71
20%-ZCOCS	8.75×10^{-10}	4.8×10^{-9}	1.36×10^{-7}	1.73

Fig. 6 (a) UV–Vis DRS of each sample; (b) $(\alpha h\nu)^2$ and $h\nu$ relation curve of CdS and $ZnCo_2O_4$; (c) PL and (d) TRPL diagrams of CdS, $ZnCo_2O_4$ and different proportion.

following triple exponential attenuation model is used for fitting:

$$I(t) = \sum_{i=1,2,3} B_i \exp(-t/\tau_i). \quad (1)$$

Meanwhile, the average life expectancy can be expressed as follows:

$$\langle\tau\rangle = \sum_{i=1,2,3} B_i\tau_i^2 \Big/ \sum_{i=1,2,3} B_i\tau_i. \quad (2)$$

The fitting results of the average life are shown in the table. The average lifetime of the composite sample is slightly shorter than that of CdS, indicating that the speed of electron transfer between the interfaces is faster. The introduction of $ZnCo_2O_4$ promotes the separation of electron–hole pairs.

3.7 Electrochemical analysis

The photoelectrochemical test is conducted to further understand the charge separation and transfer efficiency in the photocatalysis process (as shown in Fig. 7). Figure 7(a) shows the periodic photocurrent response curve of the sample, where the sample shows a good response to the periodicity of switching light. The composite sample 15%-ZCOCS shows good sensitivity and its current density is much higher than those of CdS and $ZnCo_2O_4$. This shows that the composite samples can provide more stable carriers and are easy to separate while the separation efficiency of pure samples is poor. In addition, the electrochemical impedance spectra (EIS) of the samples are measured to study the electron transfer efficiency, as shown in Fig. 7(b). In the presence of $ZnCo_2O_4$, 15%-ZCOCS has a smaller arc radius. The smaller the arc radius, the lower is the transfer resistance, and the faster is the charge transfer. All these indicate that the presence of $ZnCo_2O_4$ promotes the separation and transfer of photogenerated carriers. Figure 7(c) shows the linear sweep volt-ampere curve of the sample. In general, a lower overpotential contributes to hydrogen production [49]. The diagram shows that under the same conditions, the composite has a lower hydrogen evolution overpotential, which is more conducive to the occurrence of photocatalytic hydrogen evolution. In addition, the cyclic voltammetry (CV) curves are measured to further describe the electrochemical properties of the samples. Figures 7(d, e) show the CV curves of the sample, and the area of the CV curve represents the redox ability. Furthermore, the CV curves under the different scanning speeds are studied, and the scanning speed is found to be

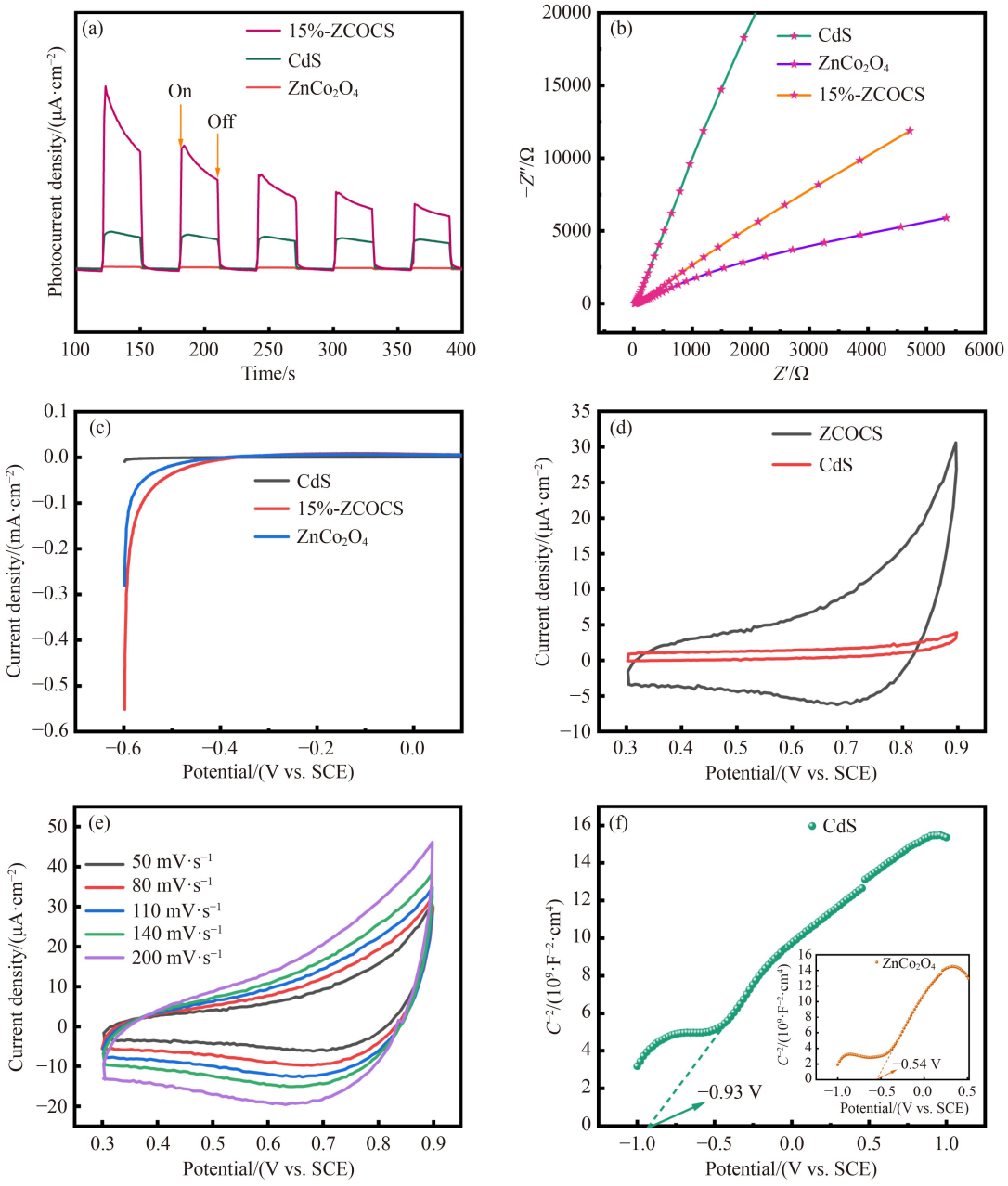

Fig. 7 (a) Transient photocurrent response; (b) EIS curves; (c) linear sweep volt-ampere curve; (d) under the window voltage of 0.3–0.9 V, the CV curves with scanning speed of 0.05 $V \cdot s^{-1}$; (e) the CV curves at different scanning rates; (f) Mott–Schottky curve.

proportional to the ring area of the CV curves [50].

In addition, the flat band potential of the catalyst is determined by conducting the Mott−Schottky test, and the position of the conduction band is determined. As shown in Fig. 7(f), compared to the saturated calomel electrode, the flat-band potentials of CdS and $ZnCo_2O_4$ are –0.93 and –0.54 V, respectively. From the tangent slope, both catalysts are n-type semiconductors. After conversion to the normal hydrogen electrode, the flat band potentials of CdS and $ZnCo_2O_4$ are –0.69 and –0.30 V, respectively. According to the characteristic of the n-type semiconductor, the flat band potential is 0.1–0.2 V higher than the conduction band potential [51,52]. As a result, the conduction band potentials of CdS and $ZnCo_2O_4$ are –0.79 and –0.4 V, respectively. According to the relationship between the band gap and the conduction band potential: $E_g = E_{VB} - E_{CB}$, where the band gaps of CdS and $ZnCo_2O_4$ are 2.32 and 1.60 eV, respectively, and their valence band potentials are 1.53 and 1.2 V.

3.8 Possible photocatalytic mechanism

As shown in Figs. 8(a, b), we conduct hydroxyl radical capture experiments on this basis.

In the experiment, terephthalic acid was mainly used to scavenge the hydroxyl radicals. The fluorescence

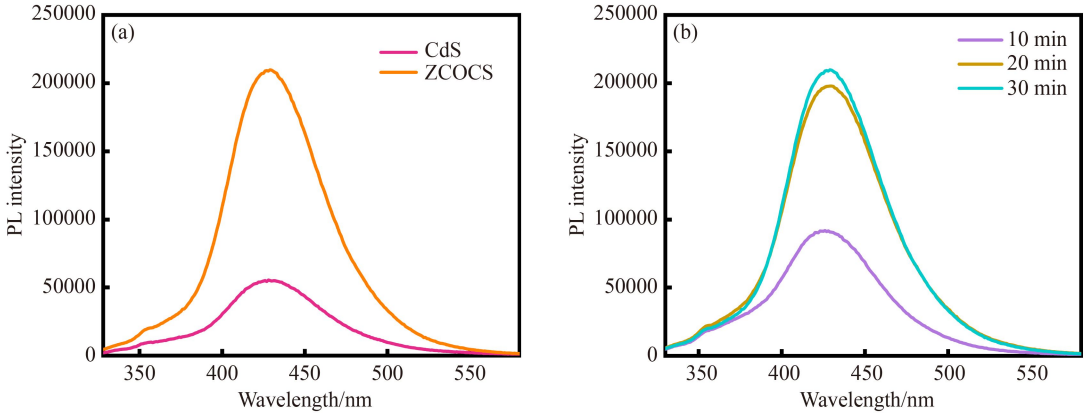

Fig. 8 (a) Fluorescence intensity of the reaction of the sample with PTA under light; (b) the variation diagram of the fluorescence intensity of the composite sample with time.

intensity indicates that the binding rate of terephthalic acid to hydroxyl radical is high, which indirectly reflects the oxidation ability of the holes. In addition, with time, the system produces more photogenerated electron–hole pairs; thus, the fluorescence intensity shows that the composite catalyst has high oxidation ability [53].

Figure 9 shows the charge transfer mechanism between CdS and $ZnCo_2O_4$. In the electrochemical tests, both CdS and $ZnCo_2O_4$ are typical n-type semiconductors. Combined with XPS, the binding energy of Cd and S elements in the composite sample is larger than that of the elements in CdS, indicating that the electron cloud density in CdS decreases. In contrast, the electron cloud density in $ZnCo_2O_4$ increases. Based on the above analysis results, the possible mechanism of hydrogen evolution is proposed. When exposed to visible light, the excitation produces electron–hole pairs. Because $ZnCo_2O_4$ has low impedance, good conductivity and close contact with CdS, the electrons in the conduction band of CdS can be quickly transferred to $ZnCo_2O_4$. At the same time, the hydrogen evolution reaction occurs on the $ZnCo_2O_4$ surface, and the useless holes in the CdS valence band are consumed by lactic acid, which effectively hinders the recombination of electron holes and makes more electrons participate in the hydrogen evolution reaction. These results show that the photocatalytic activity of the catalyst for hydrogen evolution is improved.

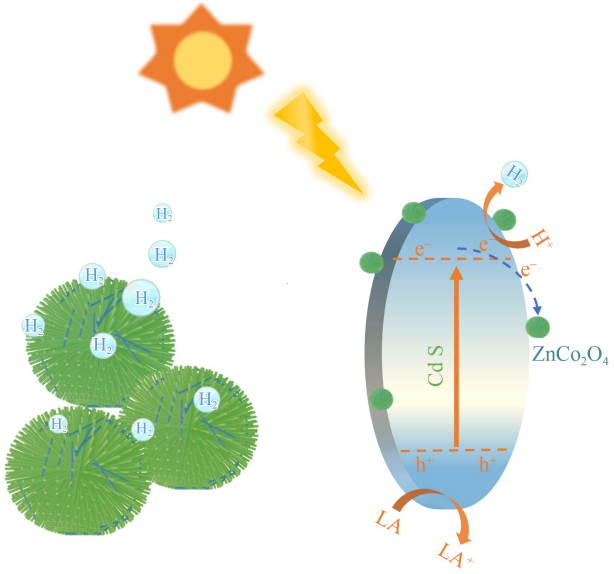

Fig. 9 Possible mechanism diagram proposed.

4 Conclusions

$ZnCo_2O_4$/CdS composites are synthesized by physical mixing, and their properties are further characterized by SEM, TEM, and XPS. Compared to the single CdS, the photocatalytic hydrogen evolution performance of the co-catalyst $ZnCo_2O_4$ modified composite is significantly improved. The photocatalytic hydrogen evolution capacity of 15% $ZnCo_2O_4$/CdS reaches 296.7 μmol, which is twice as high as that of the single CdS, and has good stability. Fluorescence shows that the addition of $ZnCo_2O_4$ accelerates the charge separation and transfer. In addition, based on the analysis results of various characterizations, the possible mechanism of photocatalytic hydrogen evolution is proposed. The results of this study show that $ZnCo_2O_4$ can be used as a good co-catalyst. Meanwhile, the study contributes to the construction of a photocatalyst with high efficiency and low cost.

Acknowledgement This work was financially supported by the National Natural Science Foundation of China (Grant No. 22062001) and the graduate innovation project of North Minzu University (Grant No. YCX22166).

References

1. Zou J, Liao G, Jiang J, Xiong Z, Bai S, Wang H, Wu P, Zhang P, Li X. *In-situ* construction of sulfur-doped g-C_3N_4/defective g-C_3N_4 isotype step-scheme heterojunction for boosting

photocatalytic H_2 evolution. Chinese Journal of Structural Chemistry, 2022, 41: 2201025–2201033
2. Wang P, Yang M, Tang S, Chen F, Li Y. Preparation of cellular C_3N_4/$COSe_2$/Ga composite photocatalyst and its CO_2 reduction activity. Chemical Journal of Chinese Universities, 2021, 6: 1924–1932
3. Yong Z, Ni Q, Long L, Bing W. Syntheses, structures and photocatalytic degradation properties of two copper(II) coordination polymers with flexible bis(imidazole) ligand. Chinese Journal of Structural Chemistry, 2021, 40: 595–602
4. Wu Y, Li Y, Zhang L, Jin Z. NiAl-LDH *in situ* derived Ni_2P and ZnCdS nanoparticles ingeniously constructed S-scheme heterojunction for photocatalytic hydrogen production. ChemCatChem, 2022, 14(4) doi:10.1002/cctc.202101656
5. Yang K, Liu T, Xiang D, Li Y, Jin Z. Graphdiyne (g-C_nH_{2n-2}) based Co_3S_4 anchoring and edge-covalently modification coupled with carbon-defects g-C_3N_4 for photocatalytic hydrogen production. Separation and Purification Technology, 2022, 298: 121564
6. Weia H, Yun M, Rong Q, Hun X, Ru L. Study on the different photocatalytic performances for tetracycline hydrochloride degradation of p-block metal composite oxides $Sr_{1.36}Sb_2O_6$ and $Sr_2Sb_2O_7$. Chinese Journal of Structural Chemistry, 2021, 40: 394–402
7. Yang Y, Wu J, Cheng B, Zhang L, Al-Ghamdi A, Wageh S, Li Y. Enhanced photocatalytic H_2-production activity of CdS nanoflower using single atom Pt and graphene quantum dot as dual cocatalysts. Chinese Journal of Structural Chemistry, 2022, 41(6): 2206006–2206014
8. Zhang L, Zhang J, Yu H, Yu J. Emerging S-scheme photocatalyst. Advanced Materials, 2022, 34(11): 2107668
9. Cao Y, Gou H, Zhu P, Jin Z. Ingenious design of Co Al-LDH p−n heterojunction based on CuI as holes receptor for photocatalytic hydrogen evolution. Chinese Journal of Structural Chemistry, 2022, 41: 2206079–2206085
10. Sayed M, Yu J, Liu G, Jaroniec M. Non-noble plasmonic metal-based photocatalysts. Chemical Reviews, 2022, 122(11): 10484–10537
11. Yan T, Zhang X, Liu H, Jin Z. CeO_2 particles anchored to Ni_2P nanoplate for efficient photo-catalytic hydrogen evolution. Chinese Journal of Structural Chemistry, 2022, 41: 2201047–2201053
12. Zhang L, Hao X, Li J, Wang Y, Jin Z. Unique synergistic effects of ZIF-9(Co)-derived cobalt phosphide and $CeVO_4$ heterojunction for efficient hydrogen evolution. Chinese Journal of Catalysis, 2020, 41(1): 82–94
13. Liu Y, Hao X, Hu H, Jin Z. High efficiency electron transfer realized over NiS_2/$MoSe_2$ S-scheme heterojunction in photocatalytic hydrogen evolution. Acta Physico-Chimica Sinica, 2021, 37(6): 2008030 (in Chinese)
14. Jin Z, Li Y, Hao X. Ni, Co-based selenide anchored g-C_3N_4 for boosting photocatalytic hydrogen evolution. Acta Physico-Chimica Sinica, 2021, 37(10): 1912033 (in Chinese)
15. Wei M, Feng L, Yan L, Lei W, Peng P, Jie Y. Dramatically enhanced visible-light-responsive H_2 evolution of $Cd_{1-x}Zn_xS$ via the synergistic effect of Ni_2P and 1t/2h MoS_2 cocatalysts. Chinese Journal of Structural Chemistry, 2021, 40: 7–22
16. Jiang Z, Chen Q, Zheng Q, Shen R, Zhang P, Li X. Constructing 1D/2D Schottky-based heterojunctions between $Mn_{0.2}Cd_{0.8}S$ nanorods and Ti_3C_2 nanosheets for boosted photocatalytic H_2 evolution. Acta Physico-Chimica Sinica, 2021, 37(6): 2009063 (in Chinese)
17. Wang G, Quan Y, Yang K, Jin Z. EDA-assisted synthesis of multifunctional snowflake-Cu_2S/CdZnS S-Scheme heterjunction for improved the photocatalytic hydrogen evolution. Journal of Materials Science and Technology, 2022, 121: 28–39
18. Li H, Gong H, Jin Z. In_2O_3-modified Three-dimensional nanoflower MoS_x form S-scheme heterojunction for efficient hydrogen production. Acta Physico-Chimica Sinica, 2022, 38(0): 2201037
19. Liu S, Wang K, Yang M, Jin Z. Rationally designed $Mn_{0.2}Cd_{0.8}S$@CoAl LDH S-scheme heterojunction for efficient photocatalytic hydrogen production. Acta Physico-Chimica Sinica, 2022, 38(7): 2109023 (in Chinese)
20. Li D, Ma X, Su P, Yang S, Jiang Z, Li Y, Jin Z. Effect of phosphating on NiAl-LDH layered double hydroxide form S-scheme heterojunction for photocatalytic hydrogen evolution. Molecular Catalysis, 2021, 516: 111990
21. Bai J, Shen R, Jiang Z, Zhang P, Li Y, Li X. Integration of 2D layered CdS/WO_3 S-scheme heterojunctions and metallic Ti_3C_2 MXene-based Ohmic junctions for effective photocatalytic H_2 generation. Chinese Journal of Catalysis, 2022, 43(2): 359–369
22. Jin Z, Li H, Li J. Efficient photocatalytic hydrogen evolution over graphdiyne boosted with a cobalt sulfide formed S-scheme heterojunctions. Chinese Journal of Catalysis, 2022, 42(2): 303–315
23. Gao R, He H, Bai J, Hao L, Shen R, Zhang P, Li Y, Li X. Pyrene-benzothiadiazole-based polymer/Cds 2d/2d organic/inorganic hybrid S-scheme heterojunction for efficient photocatalytic H_2 evolution. Chinese Journal of Structural Chemistry, 2022, 41(6): 2206031–2206038
24. Hu T, Dai K, Zhang J, Chen S. Noble-metal-free Ni_2P modified step-scheme $SnNb_2O_6$/CdS-diethylenetriamine for photocatalytic hydrogen production under broadband light irradiation. Applied Catalysis B: Environmental, 2020, 269: 118844
25. Zhang S, Du M, Xing Z, Li Z, Pan K, Zhou W. Defect-rich and electron-rich mesoporous Ti-MOFs based NH_2-MIL-125(Ti)@$ZnIn_2S_4$/CdS hierarchical tandem heterojunctions with improved charge separation and enhanced solar-driven photocatalytic performance. Applied Catalysis B: Environmental, 2020, 262: 118202
26. Wageh S, Al-Ghamdi A, Jafer R, Li X, Zhang P. A new heterojunction in photocatalysis: S-scheme heterojunction. Chinese Journal of Catalysis, 2021, 42(5): 667–669
27. Liu S, Kuang W, Meng X, Qi W, Adimi S, Guo H, Guo X, Pervaiz E, Zhu Y, Xue D, Yang M. Dual-phase metal nitrides as highly efficient co-catalysts for photocatalytic hydrogen evolution. Chemical Engineering Journal, 2021, 416: 129116
28. Shen R, Ding Y, Li S, Zhang P, Xiang Q, Ng Y, Li X. Constructing low-cost Ni_3C/twin-crystal $Zn_{0.5}Cd_{0.5}S$ heterojunction/homojunction nanohybrids for efficient photocatalytic H_2 evolution. Chinese Journal of Catalysis, 2021,

42(1): 25–36
29. Wei J, Chen Y, Zhang H, Zhuang Z, Yu Y. Hierarchically porous S-scheme CdS/UiO-66 photocatalyst for efficient 4-nitroaniline reduction. Chinese Journal of Catalysis, 2021, 42(1): 78–86
30. Peng J, Shen J, Yu X, Tang H, Zulfiqar, Liu Q. Zulfiqar, Liu Q. Construction of LSPR-enhanced 0D/2D CdS/MoO_{3-x} S-scheme heterojunctions for visible-light-driven photocatalytic H_2 evolution. Chinese Journal of Catalysis, 2021, 42(1): 87–96
31. Jia X, Wu X, Liu B. Formation of $ZnCo_2O_4$@MnO_2 core-shell electrode materials for hybrid supercapacitor. Dalton Transactions, 2018, 47(43): 15506–15511
32. Chen H, Du X, Sun J, Mao H, Wu R, Xu C. Simple preparation of $ZnCo_2O_4$ porous quasi-cubes for high performance asymmetric supercapacitors. Applied Surface Science, 2020, 515: 146008
33. Chen H, Wang J, Han X, Liao F, Zhang Y, Gao L, Xu C. Facile synthesis of mesoporous $ZnCo_2O_4$ hierarchical microspheres and their excellent supercapacitor performance. Ceramics International, 2019, 45(7): 8577–8584
34. Liang S, Sui G, Li J, Guo D, Luo Z, Xu R, Yao H, Wang C, Chen S. ZIF-L-derived porous C-doped ZnO/CdS graded nanorods with Z-scheme heterojunctions for enhanced photocatalytic hydrogen evolution. International Journal of Hydrogen Energy, 2022, 47(21): 11190–11202
35. He B, Bie C, Fei X, Cheng B, Yu J, Ho W, Al-Ghamdi A, Wageh S. Enhancement in the photocatalytic H_2 production activity of CdS NRs by Ag_2S and NiS dual cocatalysts. Applied Catalysis B: Environmental, 2021, 288: 119994
36. Raja A, Son N, Swaminathan M, Kang M. Facile synthesis of sphere-like structured $ZnIn_2S_4$-rGO-$CuInS_2$ ternary heterojunction catalyst for efficient visible-active photocatalytic hydrogen evolution. Journal of Colloid and Interface Science, 2021, 602: 669–679
37. Liu B, Cheng J, Peng H, Chen D, Cui X, Shen D, Zhang K, Jiao T, Li M, Lee C, Zhang W. *In situ* nitridated porous nanosheet networked Co_3O_4–Co_4N heteronanostructures supported on hydrophilic carbon cloth for highly efficient electrochemical hydrogen evolution. Journal of Materials Chemistry A: Materials for Energy and Sustainability, 2019, 7(2): 775–782
38. Guan S, An L, Ashraf S, Zhang L, Liu B, Fan Y, Li B. Oxygen vacancy excites Co_3O_4 nanocrystals embedded into carbon nitride for accelerated hydrogen generation. Applied Catalysis B: Environmental, 2020, 269: 118775
39. Han Y, Liang Z, Dang H, Dong X. Extremely high photocatalytic H_2 evolution of novel Co_3O_4/$Cd_{0.9}Zn_{0.1}S$ p–n heterojunction photocatalyst under visible light irradiation. Journal of the Taiwan Institute of Chemical Engineers, 2018, 87: 196–203
40. Wang L, Tang G, Liu S, Dong H, Liu Q, Sun J, Tang H. Interfacial active-site-rich 0D Co_3O_4/1D TiO_2 p−n heterojunction for enhanced photocatalytic hydrogen evolution. Chemical Engineering Journal, 2022, 428: 131338
41. Liu J, Ke J, Li Y, Liu B, Wang L, Xiao H, Wang S. Co_3O_4 quantum dots/TiO_2 nanobelt hybrids for highly efficient photocatalytic overall water splitting. Applied Catalysis B: Environmental, 2018, 236: 396–403
42. Li H, Wang G, Zhang X, Jin Z. Based on amorphous carbon C@$Zn_xCd_{1-x}S$/Co_3O_4 composite for efficient photocatalytic hydrogen evolution. International Journal of Hydrogen Energy, 2020, 45(15): 8405–8417
43. Ma B, Liu Y, Li J, Lin K, Liu W, Zhan H. Mo_2N: an effificient non-noble metal cocatalyst on CdS for enhanced photocatalytic H_2 evolution under visible light irradiation. International Journal of Hydrogen Energy, 2016, 41(47): 22009–22016
44. Penga J, Xu J, Wang Z, Ding Z, Wang S. Developing an efficient $NiCo_2S_4$ cocatalyst for improving visible light H_2 evolution performance of Cds nanoparticles. Physical Chemistry Chemical Physics, 2017, 19(38): 25919–25926
45. Ma B, Xu H, Lin K, Li J, Zhan H, Liu W, Li C. Mo_2C as non-noble metal co-catalyst in Mo_2C/CdS composite for enhanced photocatalytic H_2 evolution under visible light irradiation. ChemSusChem, 2016, 9(8): 820–824
46. Tian L, Min S, Wang F, Zhang Z. Metallic vanadium nitride as a noble-metal-free cocatalyst efficiently catalyze photocatalytic hydrogen production with CdS nanoparticles under visible light irradiation. Journal of Physical Chemistry C, 2019, 47(47): 28640–28650
47. Meng X, Qi W, Kuang W, Adimi S, Guo H, Thomas T, Liu S, Wang Z, Yang M. Chromium-titanium nitride as efficient co-catalyst for photocatalytic hydrogen production. Journal of Materials Chemistry A: Materials for Energy and Sustainability, 2020, 8(31): 15774–15781
48. Mao M, Xu J, Li J, Zhao S, Li X. Enhancement of catalytic hydrogen evolution by NiS modification of $ZnCo_2O_4$ with cubic morphology. Journal of Materials Science: Materials in Electronics, 2020, 31(15): 12026–12040
49. Gong H, Zhang X, Wang G, Liu Y, Li Y, Jin Z. Dodecahedron ZIF-67 anchoring ZnCdS particles for photocatalytic hydrogen evolution. Molecular Catalysis, 2020, 485: 110832
50. Wang G, Jin Z. Oxygen-vacancy-rich cobalt-aluminium hydrotalcite structures served as high-performance supercapacitor cathode. Journal of Materials Chemistry C: Materials for Optical and Electronic Devices, 2021, 9(2): 620–632
51. Jin Z, Wang X, Wang Y, Yan T, Hao X. Snowflake-like Cu_2S coated with NiAl-LDH forms a p–n heterojunction for efficient photocatalytic hydrogen evolution. ACS Applied Energy Materials, 2021, 4(12): 14220–14231
52. Quan Y, Wang G, Jin Z. Tactfully assembled CuMOF/CdS S-scheme heterojunction for high-performance photocatalytic H_2 evolution under visible light. ACS Applied Energy Materials, 2021, 4(8): 8550–8562
53. Li J, Li M, Jin Z. 2D/3D ZIF-9/$Mo_{15}S_{19}$ S-scheme heterojunction for productive photocatalytic hydrogen evolution. Energy Technology, 2022, 10(2): 2100669